buildings

MDPI

Article

Analysis of Gravel Migration Patterns During Vibration Rolling and Their Impact on GCL Performance Based on DEM

Hu Huang [1], Feihao Chen [1], Qingming Qiu [2,*], Ruihang Li [1] and Lixia Guo [1]

[1] School of Water Conservancy, North China University of Water Resources and Electric Power, Zhengzhou 450046, China; huanghu@ncwu.edu.cn (H.H.); x202210010027@stu.ncwu.edu.cn (F.C.); x20231010030@stu.ncwu.edu.cn (R.L.); guolixia@ncwu.edu.cn (L.G.)
[2] School of Civil Engineering, Tianjin University, Tianjin 300072, China
* Correspondence: lemoncc_717@tju.edu.cn

Abstract: In this study, a multilayer composite rolling model consisting of a rolling wheel, a protective layer, a GCL, and a support layer was constructed by the discrete element method (DEM). Soil compaction and gravel migration, and their effects on the GCL, were analyzed from a fine viewpoint, and three key indexes for the safety assessment of the GCL were proposed: local elongation, gravel embedment value, and bentonite allotment number. The results show that the soil porosity and cumulative settlement do not decrease all the time with the number of rolling passes, and there exists an optimal number of rolling passes during the rolling process; the protective layer of gravel soil moves more frequently than the support layer; and the nearly rectangular and nearly elliptical gravels are more likely to rotate. The maximum local elongation of the GCL was 3.79% during the lapping process, and all gravels in contact with the upper boundary of the GCL extruded the GCL to varying degrees during the lapping process. The distribution of bentonite particles is closely related to the contact mode between gravel and GCL.

Keywords: bentonite distribution; construction compaction; discrete element method; gravel embedding value; lime-mixed gravel soil; particle migration

check for updates

Citation: Huang, H.; Chen, F.; Qiu, Q.; Li, R.; Guo, L. Analysis of Gravel Migration Patterns During Vibration Rolling and Their Impact on GCL Performance Based on DEM. *Buildings* **2024**, *14*, 3640. https://doi.org/10.3390/buildings14113640

Academic Editor: Pramen P. Shrestha

Received: 10 October 2024
Revised: 6 November 2024
Accepted: 12 November 2024
Published: 15 November 2024

Copyright: © 2024 by the authors. Licensee MDPI, Basel, Switzerland. This article is an open access article distributed under the terms and conditions of the Creative Commons Attribution (CC BY) license (https://creativecommons.org/licenses/by/4.0/).

1. Introduction

In landscape river channel regulation projects, artificial impermeable materials such as geosynthetic clay liners (GCLs) and geomembranes are usually arranged on the riverbed foundation, and lime-treated soil, well-graded soil, or sand–gravel mixes are used as the support and protective layers of impermeable materials to meet water storage needs. To improve the utilization rate of local materials, save engineering costs, and protect the ecological environment during construction, excavated materials from rivers can be directly used as support and protective layers of impermeable materials. However, due to the characteristics of natural excavated materials, such as those with poor gradation and irregular particle shapes, especially in areas with a high gravel content, there are fewer studies related to the direct use of excavated materials as the support and protective layers of impermeable materials. The influences of compaction characteristics and the rolling process on the impermeable material are worthy of further study.

According to relevant projects in China and other countries, cement mortar, clay, etc., with good particle gradation and smooth particles are commonly used with a GCL as support and protective layers [1–4]. These material particles have regular boundaries and smooth contacts with the GCL, and will not squeeze or puncture the GCL and geomembrane, which is widely used in engineering. However, certain areas are unable to obtain the above materials for a project due to the lack of local soil materials, inconvenient transportation, project investment restrictions, and environmental factors [5]. Many scholars have studied the failure mechanism on the contact surface of the GCL and the adjoining material [6–8]. Pillai and Gali (2022) [9] learned from a direct shear test of the interface

between a GCL and sand particles that the shear strength of the interface is influenced by the surface properties of the GCL, the size and shape of the sand particles, and other factors. Hou et al. [10] simulated the initial state and loading process of geomembrane-lined soil with discrete element method (DEM) software, and analyzed the motion characteristics and mechanical properties of soil. Pillai and Gali [11] studied the surface changes of GCL samples through image binarization analysis and confirmed the influence of particle shape on interface shear response. The above research results indicate that a feasibility study of gravel soil with poor gradation as a GCL protective layer and support layer material is still lacking, and there is not sufficient theoretical guidance for related projects.

Irregular gravel soil from river excavation can be used as a protective and support layer for GCL by mixing a certain amount of lime to improve the recycling rate of excavated waste materials. Mechanical rolling is commonly used in river channel seepage control projects to compact the backfill layer; however, the spatial position change of irregular gravel in the compaction process may have some influence on GCL. The most direct and effective method for the study of vibratory rolling problems is the prototype test, but due to the limitations of the required time, high investment, large consumables, variable weather, and poor repeatability, most research is realized by numerical simulation. At present, some scholars have used simulation technology to simulate impermeable materials, which has important reference significance for the modeling method of the GCL and the value of mesoscopic parameters in this study. Domestic and foreign scholars mostly use the DEM for research [12–15], in which the simulation method of the compaction machinery and the compacted material, the selection of the material contact model, and the determination of mesoscopic parameters are the key to determining the success of the numerical simulation. Li et al. [16] used a short plate composed of several side-by-side rigid particle clump units to simulate the roller. According to the rolling mechanical parameters, the wheel weight and excitation force were applied for the short plate, and the engineering practice was preliminarily restored. In a follow-up study, Pei and Yang [17] simplified the roller as a solid cylinder rolling at a constant velocity and studied the change in foundation compaction stress under geogrid reinforcement conditions. Acquah and Chen [18] used DEM simulation technology to simulate the process of wheel rolling of soil and found that factors such as the shape of the wheel, volume density, and rolling resistance can affect rolling. Chen et al. [19] established a finite element–discrete element coupled rolling model to simulate the real shape of the roller by finite element software. Hu et al. [20] established a rolling simulation model of tire–ground interaction based on the DEM and made a refined simulation of the concave and convex ridges on the tire surface to restore the contact changes of the tire rolling along pavement under real conditions. Most of the above research results finely simulate the shape of the roller, which fails to reflect the excitation force of the compaction machinery in the working process; alternatively, the roller is simplified as a rolling plate, and exciting force is applied to it, but this fails to reflect the kneading effect of the roller on the material. Therefore, the simulation of the roller should not only reflect the kneading effect on the ground material, but also give the exciting force to reflect the vibration effect. To solve this problem, Liu et al. [21] established a quantitative relationship between the size of different rollers and the applied load, and proposed a simulation method for the equivalent load of the roller, which further solved the conversion relationship between the actual roller and the simulated roller when using simulation technology to study the rolling problem.

To improve the accuracy of the vibration rolling construction model, it is necessary to calibrate the mesoscopic parameters of the compacted material to fully reveal the compaction characteristics and particle migration of the material under a vibration rolling load. At present, scholars worldwide mainly reproduce the rolling test and indoor mechanical performance test via simulation, calibrate the mesoscopic variables such as the aggregate boundary and contact model variables, and obtain theoretical results that are helpful for the simulation of vibration rolling tests. Liu et al. [22] used DEM simulation technology to simulate the rolling process of rockfill dam construction. Laser scanning was

performed on the coarse aggregate, and an aggregate model with an irregular boundary was established. Taking the cumulative settlement of the material in actual dam construction as the calibration target, the mesoscopic parameters of the material were calibrated. Liu et al. [23] determined the detailed parameters for the epoxy asphalt mixture roller compaction model based on the back-propagation neural network trial calculation method of the field Superpave gyratory compaction test. Currently, most of the test materials in compaction modeling are rockfill, crushed concrete, or asphalt mixtures, and there is a lack of field compaction tests on lime-mixed gravel soils. Research on the mesoscopic parameters of coarse-grained soil such as sand and sandy gravel soil is relatively mature worldwide. Lu et al. [24] established a DEM model for the triaxial compression testing of sandy pebble soil with different coarse grain contents. With the actual test results, the mesoscopic parameters determined were the contact modulus, friction coefficient, and contact bond strength. Nie et al. [25] used DEM to study the dynamic characteristics of gravel–sand mixtures, and established a cyclic compression test model for irregular gravel. Tu et al. [26] established a DEM direct shear test model considering the actual shape and fracture characteristics of gravel. The accuracy of the simulation model was improved by calibrating the mesoscopic parameters based on the test data. The above research on the mesoscopic parameters of sand and gravel soil materials has achieved good results, but research on the mesoscopic parameters of lime-mixed gravel soil is still very limited. Nevertheless, such works represents an efficacious method for calibrating lime-mixed gravel soil in conjunction with its mechanical property tests.

The objective of this study was to assess the feasibility of using irregular aggregates excavated from river and waste materials in engineered impermeable protection and support layers. An indoor triaxial test was carried out using soil excavated from the site as test material. Based on the results of the triaxial compression test and the criteria of GCL, the mesoscopic parameters of the roller compaction model were calibrated, which in turn led to the development of a DEM simulation model of vibratory roller compaction for the structure of the support layer of the lime-mixed gravel soil–GCL–protective layer of lime-mixed gravel soil. The macroscopic mechanical properties of the GCL were examined in depth, and its mesoscopic mechanism was revealed by the DEM technique; the dynamic migration of the GCL under vibratory compaction load was studied, and the migration trend was revealed; and three indexes, namely, local elongation of the GCL, embedment value of the gravel, and coordination number of the bentonite, were proposed to evaluate the effect of the irregular gravels on the GCL in the process of compaction by the vibratory roller. The research results have certain practical significance in saving resources, reducing engineering costs, and protecting the environment, and can provide a strong theoretical reference for similar engineering construction.

2. Experiment

2.1. Test Specimen

The soil materials and lime were obtained from Linzhou City, Henan Province, China, and the proportions of each material particle size are detailed in Figure 1. Figure 1 shows that the gravel soil contains more fine and coarse gravel particles, with a lower proportion of medium-size particles and a large pore volume. The uniformity coefficient and curvature coefficient of the soil were calculated by Equations (1) and (2):

$$C_u = \frac{d_{60}}{d_{10}} \tag{1}$$

$$C_c = \frac{{d_{30}}^2}{d_{60} \times d_{10}} \tag{2}$$

where C_u is the uniformity coefficient, C_c is the curvature coefficient, and d_{60}, d_{30}, and d_{10} are 60%, 30%, and 10% of the total mass of soil smaller than this particle size in the grading curve, respectively.

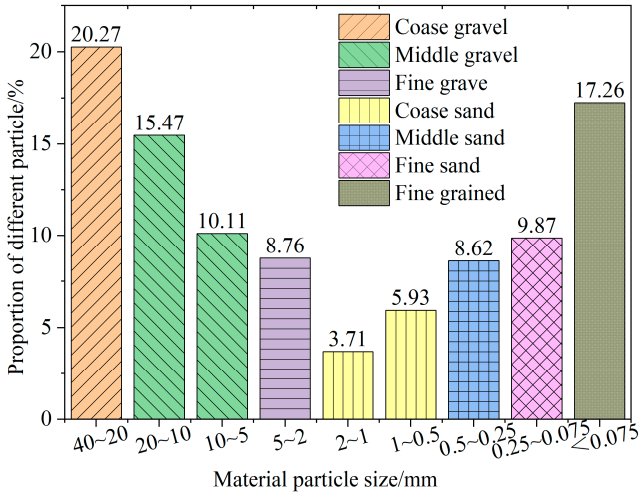


Figure 1. The proportions of test material particle sizes.

Figure 2 shows the grading curve of the soil used. It can be seen from Figure 2 that d_{60} is 7.5 mm and that d_{30} is 0.32 mm. Since the corresponding particle size of d_{10} cannot be determined, the minimum particle size of the sample is 0.075 mm, and the particle size of the interval where d_{10} is located must be less than 0.075 mm, that is, the maximum value is 0.075 mm. After calculation, C_u is 100 and C_c is 0.18. When $C_u \geq 5$ and $C_c \leq 1$, the soil sample is poorly graded soil.

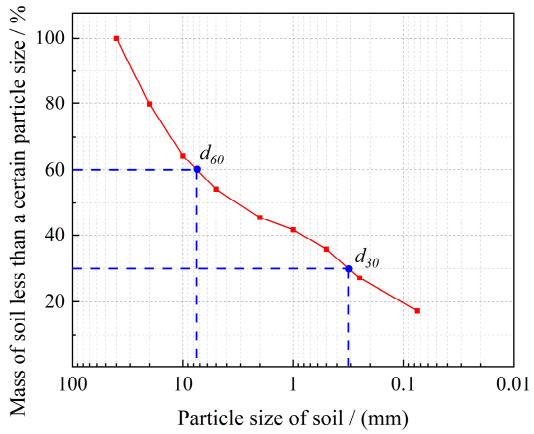


Figure 2. Field soil grading curve.

The samples for the triaxial compression test of lime-mixed gravel soils were prepared using a heavy-duty compactor, with three samples per group of ϕ 150 × 300 mm in size, as required by the Mechanical Properties of Cemented Sands and Gravels Test Procedure, T/CHINCOLD 002-2021. The compaction test was carried out by adding 8% slaked lime (lime-to-gravel soil mass ratio) to the pebbly soil, and the maximum dry density of the lime-mixed gravel soil was determined to be 2.13 g/cc, corresponding to an optimum moisture content of 5%. The preparation process is shown in Figure 3.

The specific steps are as follows: (1) Add lime to the soil material and mix well. (2) The moisture content of the sample is the optimal moisture content. Add a predetermined amount of water to the soil sample, mix uniformly, and seal it for 12 h to allow it to sufficiently react. (3) Apply lubricating oil to the compacting mold, put the soil sample into the mold in three layers. The compaction ratio is controlled at 0.93, each layer is compacted 56 times, and the upper surface is chiseled after compaction, so that the soil materials of each layer are firmly combined and the soil sample is compacted. (4) Remove the soil sample and wrap it with cling film, and carry out the triaxial compression test after 7 days of maintenance.

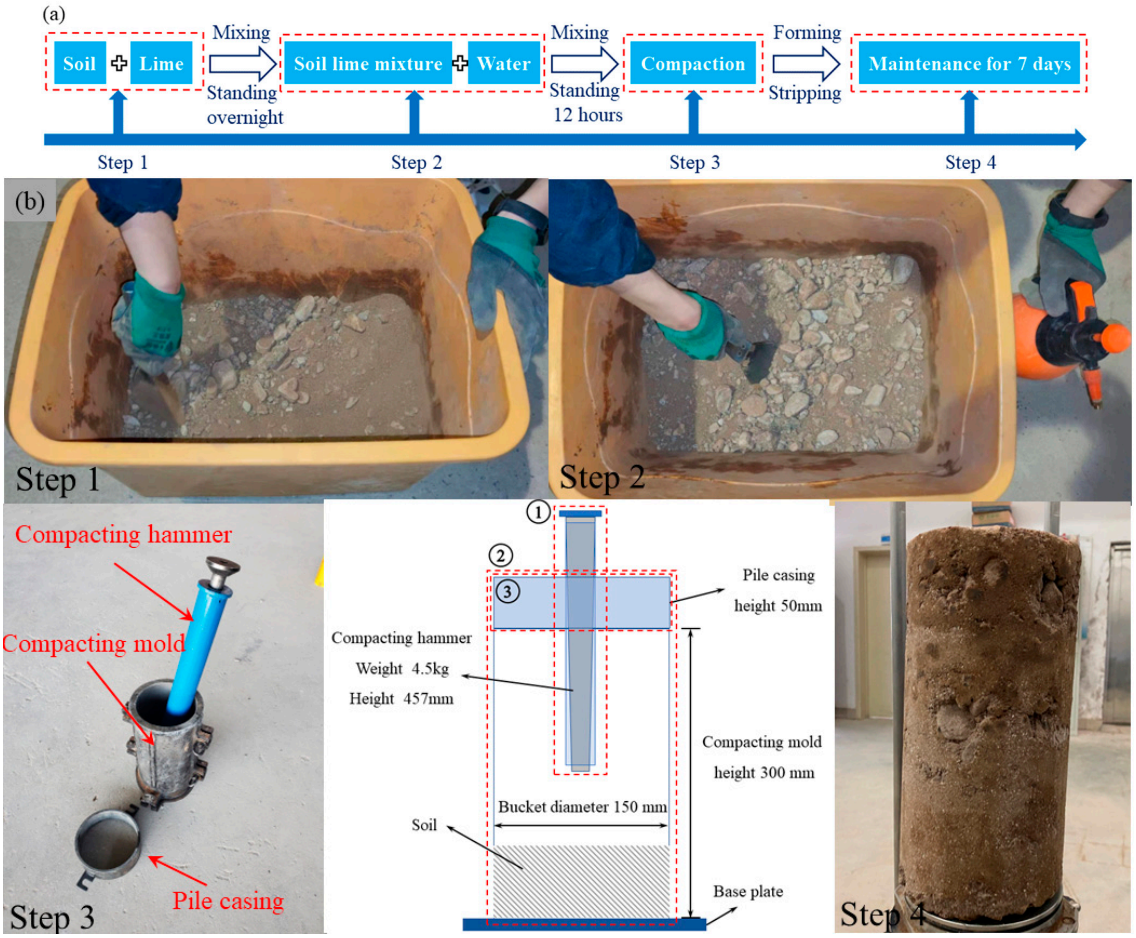


Figure 3. Triaxial compression test sample preparation process: (**a**) sample preparation steps; (**b**) sample preparation process.

2.2. Triaxial Compression Test

A STX-600 triaxial compression apparatus (Figure 4), produced by GCTS, Tempe, AZ, USA, was used to carry out unconsolidated undrained triaxial compression tests on lime-mixed gravel soils at different confining pressures (50 kPa, 100 kPa, and 150 kPa), and the loading rate was controlled by strain during the tests (the loading was stopped when the strain reached approximately 10%). The middle value of each group of three specimens was taken as the test result for that group of specimens, and the tests are shown in Figure 5.

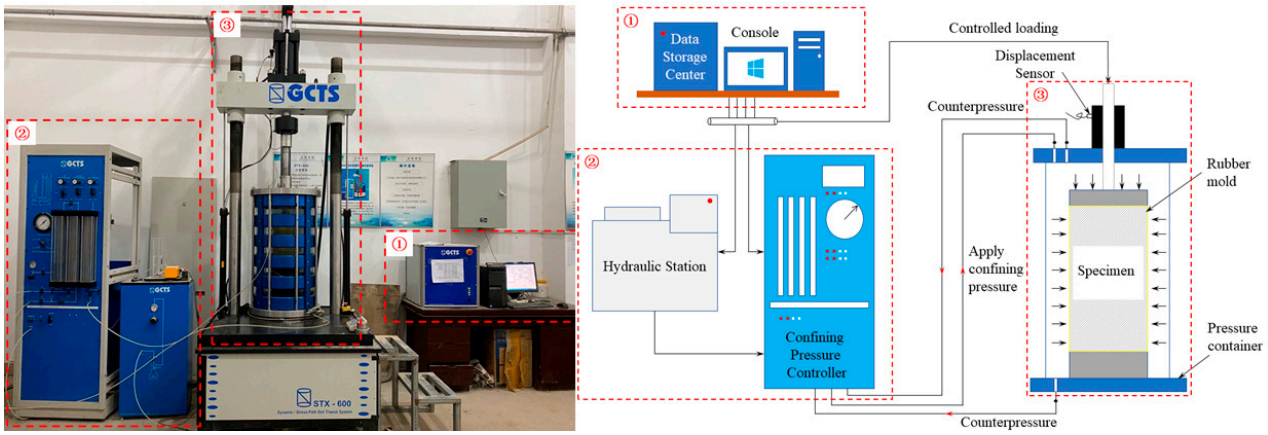


Figure 4. Test equipment.

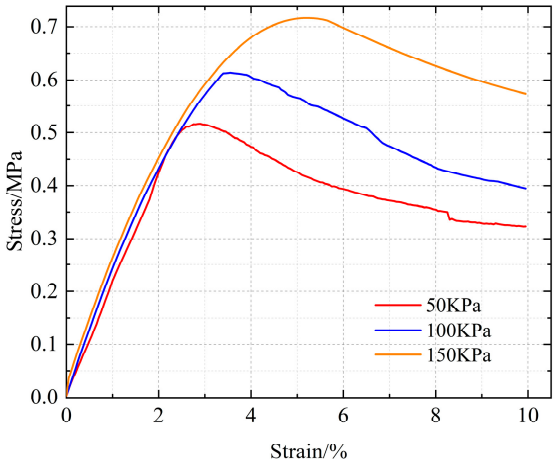


Figure 5. Stress-strain curves of lime-mixed gravel soil under different confining pressures in the triaxial compression test.

Figure 5 shows that the stress-strain curves of lime-mixed gravel soil under different confining pressures are the same: at the initial stage of loading, the curve shows a linear trend; with increasing stress, the curve shows a nonlinear trend. After reaching the peak stress, the curve decreases slowly. The stress-strain curve can be divided into the elastic deformation stage, plastic deformation stage, and failure stage. When the confining pressure is small, the elastic stage is dominant, and the plastic deformation trend gradually appears with increasing confining pressure. Under different confining pressures (50 kPa, 100 kPa, and 150 kPa), the maximum stress of the elastic stage is 92%, 90%, and 73% of the peak stress, respectively. In addition, the strength of lime-mixed gravel soil increases with increasing confining pressure. In the elastic deformation stage, the rising rate of the stress-strain curve is large, and the soil particles are in the extrusion state; in the plastic deformation stage, the stress rising rate decreases, and further compression leads to the relative dislocation between particles and microcracks. In the failure stage, the microcracks inside the specimen are connected, and the overall cementation ability of the specimen is gradually lost, so that the stress-strain curve decreases slowly under the action of confining pressure.

3. Establishment of the Rolling Construction Model

3.1. Simulation of the Equivalent Load of Roller

In this study, the clump unit was used to simulate the roller, and an equivalent load calculation method presented in the literature [21] was used to apply an excitation force to restore the actual working condition of the roller and fully simulate the characteristics of the soil material being kneaded and rearranged to fill gaps during the rolling process.

The equivalent load can be determined from Equation (3) [21]:

$$\begin{cases} \frac{F_s}{G_s} = \frac{F_r}{G_r} \\ \frac{G_s}{G_r} = \frac{F_s}{F_r} = K \cdot \beta, \text{ and } \beta = \left(\frac{D_s}{D_r}\right)^{0.5} \cdot \frac{B_s}{B_r} \end{cases} \tag{3}$$

where F_S, G_S, D_S, and B_S represent the excitation force, static load, roller width, and roller diameter in the numerical simulation, respectively. F_r, G_r, D_r, and B_r represent the excitation force, static load, width, and diameter of the actual roller. K is the correction factor.

K can be expressed by Equation (4) [21]:

$$K = 1.431 - 0.428\left(\frac{D_s}{D_r}\right)^3 \tag{4}$$

The performance parameters of the vibratory roller used in construction are shown in Table 1.

Table 1. Main performance parameters of rolling machinery.

Roller Weight (t)	Roller Width (m)	Roller Diameter (m)	Vibration Frequency (Hz)	Exciting Force (kN)	Operating Speed (km/h)
13	2.17	1	33	404	5

According to Equations (3) and (4), the equivalent load of the excitation force was calculated. The specific calculation results are shown in Table 2. The calculated equivalent excitation force was applied to the roller together with the weight of the roller by writing commands. The angular velocity of the roller was determined by the operating speed and the radius of the roller, which was calculated by the following formula:

$$\omega = v / \frac{D_s}{2}.$$

Table 2. Calculation table of equivalent load and other parameters of roller diameter for the simulation model.

D_S (m)	D_S/D_r	K	F_r (kN)	F_s (kN)	Vibration Frequency (Hz)	Operating Speed (km/h)	Angular Velocity (rad/s)
1	0.46	1.389	118.523	111.766	33	5	10

3.2. Refined Simulation Method of Irregular Gravels

Gravel soils in river excavations consist mainly of gravel and fine-grained soils. The shape of natural gravel is irregular, and when only spherical particles are used to simulate gravel soil, it is difficult to distinguish between gravel and fine-grained particles, and it cannot fully reflect the effect of gravel on GCL in the actual state. Therefore, as shown in Figure 6, gravel is simulated with particle clump elements with irregular boundaries, and closed gravel contour lines are obtained by two-dimensional processing according to the characteristics of gravel, and then generate particle clumps in the irregular boundaries. The sampling process of the gravel model is shown in Figure 7.

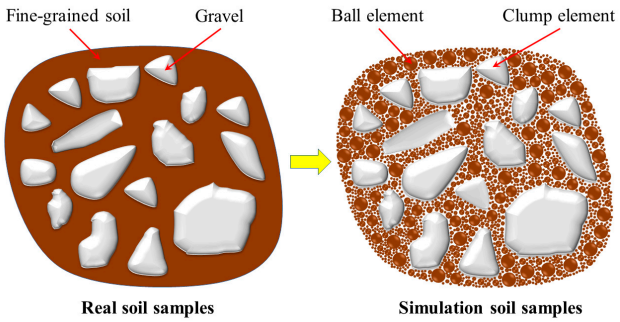


Figure 6. Simulation method of gravel soil.

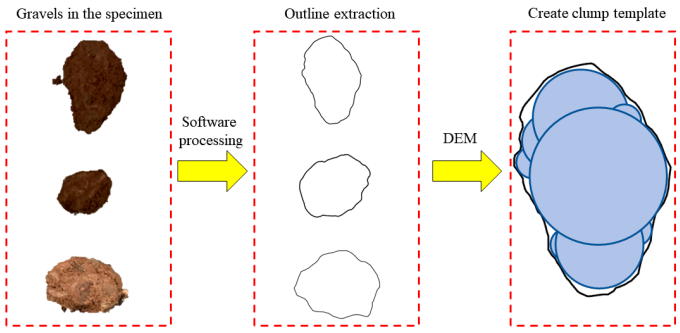


Figure 7. The process of simulating gravels.

3.3. Modelling Procedure

Figure 8 shows a schematic diagram of the vibration rolling model with the site backfill construction plan. As shown in Figure 8a, the lower layer is a 0.3 m thick lime-mixed gravel soil support layer, the middle layer is a 0.005 m thick GCL layer, and the upper layer is a 0.3 m thick lime-mixed gravel soil protective layer. In the simulation, the thickness of each layer of material is consistent with that at the construction site, and the length of each layer of material is 2 m. The particle gradation of the lime-mixed gravel soil is shown in Figure 9. The maximum particle size is 40 mm. To improve the calculation efficiency of the model, the minimum particle size is 5 mm. The process of rolling model establishment is shown in Figure 8b. The site backfill construction process is shown in Figure 8c.

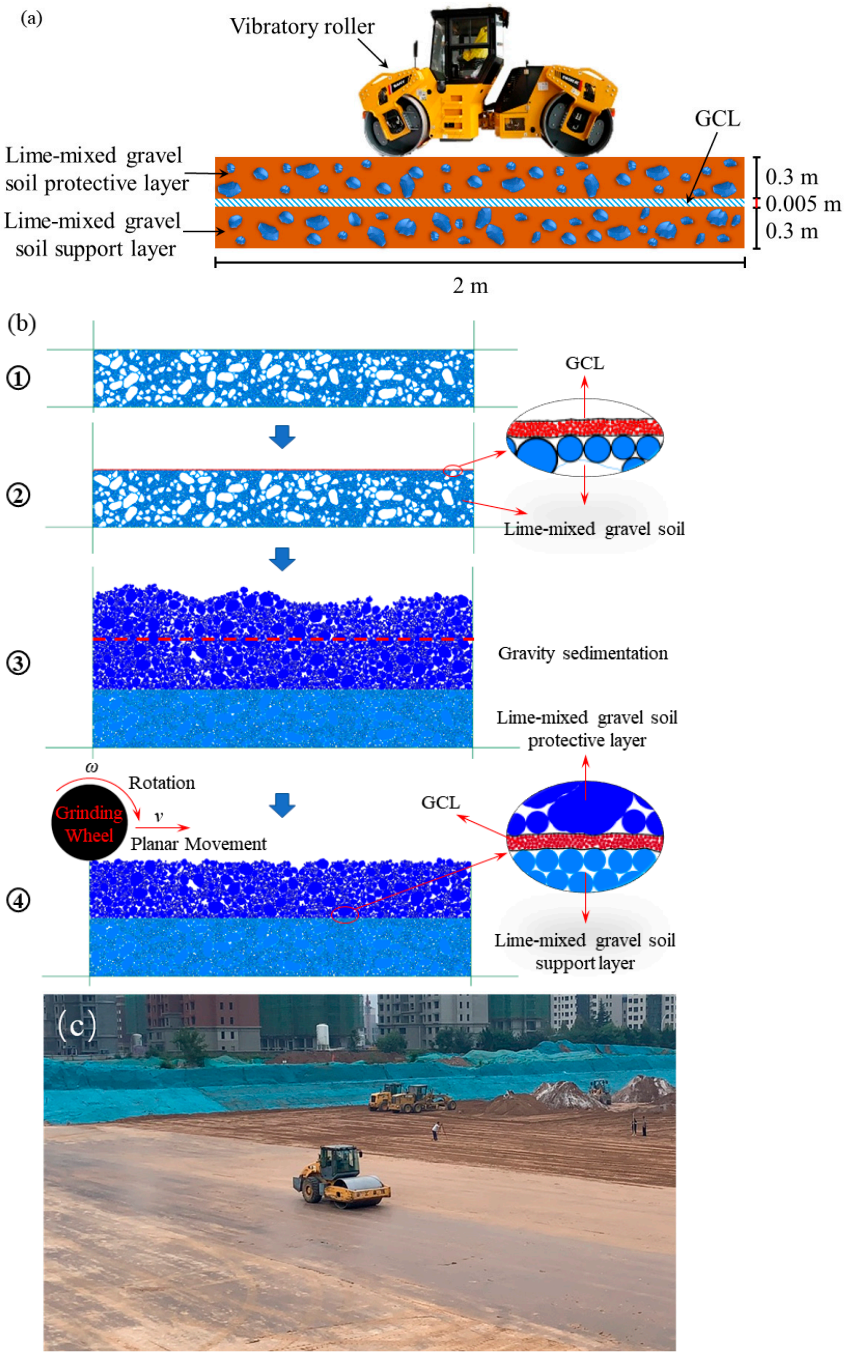


Figure 8. Vibration rolling model schematic diagram with site construction drawings: (**a**) construction diagram; (**b**) modeling process; (**c**) backfill construction drawings.

The generation steps of the support layer are as follows: (1) according to the particle gradation curve, the spherical particles are randomly placed within the boundary range, and the model is balanced after calculation; (2) the coordinate positions of the spherical particles with a particle size greater than 10 mm are obtained and recorded, these particles are deleted, and the corresponding rigid particle cluster units are placed at the original coordinates; and (3) the operation is ended after the model is balanced. For the GCL layer, two rigid boundaries are generated above the first layer. After filling the particles, the boundary is deleted, and two rows of small ball particles are generated in the original position to simulate the flexible boundary of the GCL. After the generation is completed, gravity is applied to the model to naturally settle to the lime-mixed gravel soil support layer, and the gravity is removed after the balance. The generation method of the protective layer is consistent with steps 1 and 2 of the support layer. When step 3 is carried out, gravity should be applied to allow free settlement to simulate the backfilling process during construction; after settling is completed, the excess particles are removed, the boundary is leveled and the roller is established, and the roller weight and excitation force are given equivalent loads to prepare for rolling.

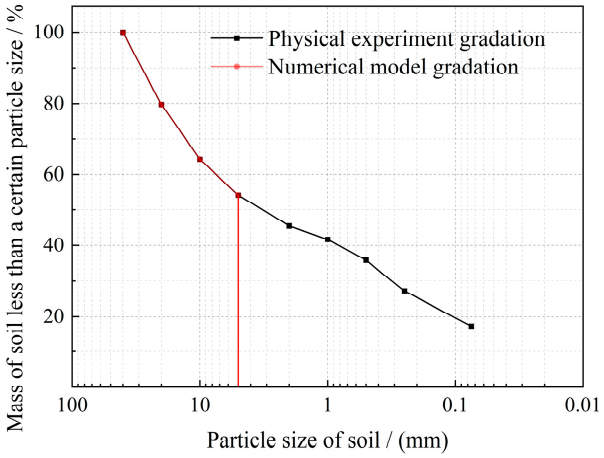


Figure 9. Simulation model gradation curve.

3.4. Mesoscopic Parameter Calibration Process of Lime-Mixed Gravel Soil and GCL

3.4.1. Calibration of the Mesoscopic Parameters of Lime-Mixed Gravel Soil

A certain amount of lime was added to the gravel soil, and then a certain amount of water was added. The hydration reaction between lime and water will generate cementation. Therefore, the cementation properties of the material need to be considered in the simulation process. The test material used in the literature [27,28] contains many cements. In the simulation process, the linear parallel bond (PB) model is selected, and the simulation results are in good agreement with the experimental results. Therefore, the PB model was selected as the mesoscopic contact model of lime-mixed gravel soil. Figure 10 shows the DEM simulation model and simulation results of the triaxial compression test for lime-mixed gravel soil. As shown in Figure 10a, gravels with irregular boundaries were simulated by rigid particle clump elements (see Section 3.2 for the specific sampling method), and fine-grained soil and lime were simulated by rigid spherical particles; several spherical particles were generated on the two sides of the sample boundary, and the contact model there was used to bond the rigid spherical particles to simulate the rubber film.

Figure 10b shows that the simulation results of the stress-strain curve of the triaxial compression test of the lime-mixed gravel soil are in good agreement with the test results. The maximum error between the simulation results of the peak stress of the sample under different confining pressures and the test results is only 2.3%, which can meet the engineering accuracy requirements, indicating that the calibrated mesoscopic mechanical parameters of lime-mixed gravel soil can accurately characterize its macroscopic mechanical

properties. The mesoscopic mechanical parameters of lime-mixed gravel soil are detailed in Table 3.

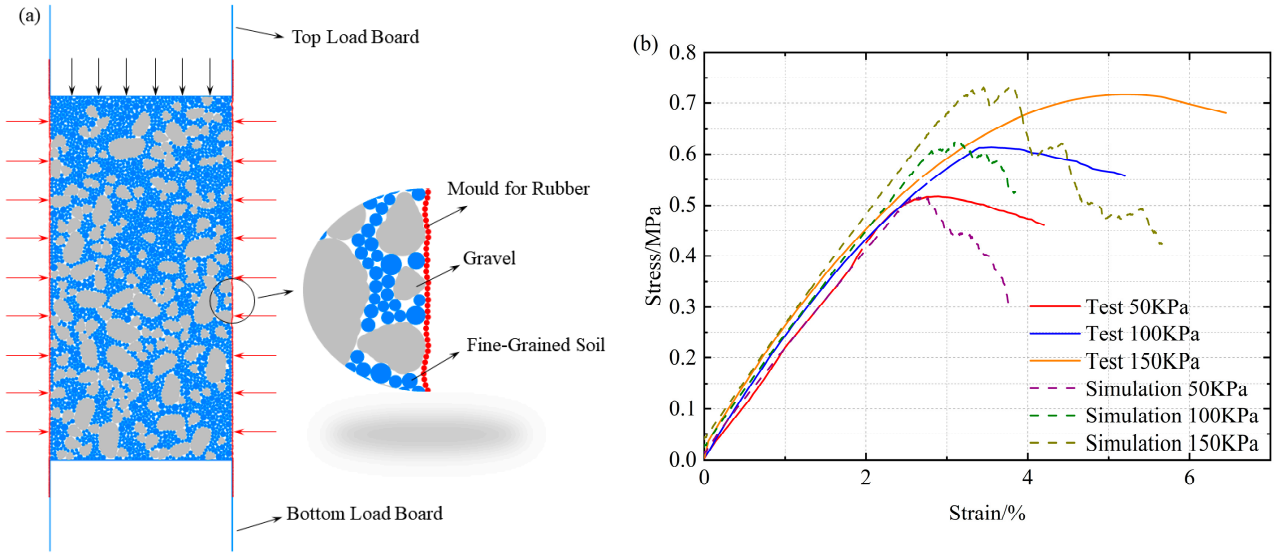


Figure 10. Triaxial compression test: (**a**) numerical simulation model; (**b**) numerical simulation results and test results comparison diagram.

Table 3. Mesoscopic parameters of lime-mixed gravel soil and GCL.

	E^*	k_n/k_s	μ	$\overline{E}^*$	$\overline{k}_n/\overline{k}_s$	$\overline{\sigma}_c$	$\overline{c}$	T_F	S_F
Fine-grained soil	1.4×10^7	1.5	0.7	1.4×10^7	1.5	8.4×10^5	8.4×10^5	-	-
Gravel	1.4×10^7	1.5	0.7	-	-	-	-	-	-
GCL boundary	2×10^7	0.5	0.7	-	-	-	-	1×10^4	1×10^4
Bentonite	1×10^7	0.5	0.7	-	-	-	-	-	-

3.4.2. Calibration of Mesoscopic Parameters of GCL

The GCL is made by wrapping sodium bentonite particles in two layers of geotextile. Bentonite particles in the anhydrous state without cementation were modeled using a linear model, and geotextiles were modeled using a linear contact bond model. Considering that the vibration rolling load will affect the force transfer of the GCL to the lower soil, the PB model is used as the constitutive model of the contact between the boundary of the GCL and the upper and lower soil. The model schematic and simulation results are shown in Figure 11.

The standard "Sodium bentonite geosynthetic clay liner" [27] indicates that the elongation of the GCL under the maximum load is greater than 10%, which can meet the engineering requirements, and the elongation is calculated by Equation (5) [28]:

$$\varepsilon_{max} = \frac{\Delta L - L_0'}{L_0} \times 100 \quad (5)$$

where $\varepsilon_{\max}$ is the elongation at maximum load, ΔL is the elongation length at maximum load, L_0' is the elongation length at preload, and L_0 is the initial length.

Figure 11b shows that the elongation under maximum load is greater than 14%, which meets the requirements of the standards. The mesoscopic parameters of the GCL are given in Table 3.

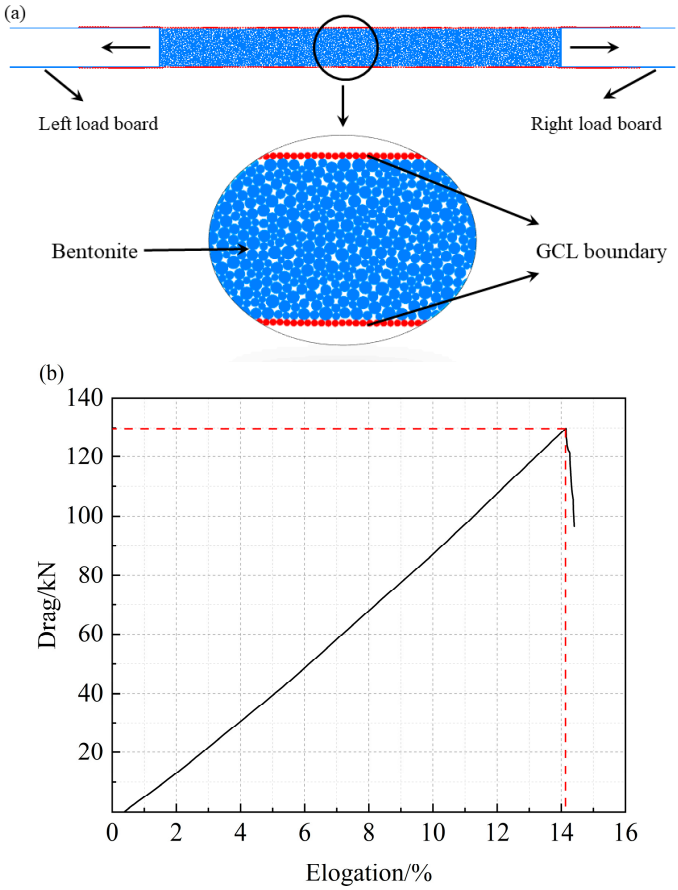


Figure 11. Calibration process of the GCL: (**a**) GCL tensile test model; (**b**) test results.

4. Analysis of the Simulation Results

4.1. Analysis of the Porosity and Cumulative Settlement

Figure 12 shows the graphs of porosity and cumulative settlement with an increasing number of rolling passes. As shown in Figure 12, when the soil is balanced and stabilized under the action of self-weight, the initial porosity of the model is 13.5%, and the porosity is stabilized at approximately 12.6% at the end of 15 vibratory rolling passes. The cumulative settlement increases gradually with increasing rolling passes. The whole simulated compaction process can be divided into three stages. The first stage is 1–4 passes, when the porosity decreases significantly with increasing rolling passes and the pore reduction rate decreases gradually. This is due to the loose material properties when it is not rolled, and there are many voids between the gravels and soil particles. Under the action of a vibratory rolling load, the fine particles fill the voids so that the particles are in closer contact with each other. The second stage is 5–9 passes, when the porosity tends to be stable and then decreases slowly with increasing rolling passes, reaching a minimum value of 12.58% at the 9th rolling. The third stage is 10–15 passes, when the porosity rises slightly and then tends to stabilize, indicating that there is an optimal number of passes in the rolling process. When making the optimal number of rolling passes, the material reaches the design density, particles cannot absorb excess energy from the rolling vibration, and the energy generated from the vibrations is transferred to the elastic strain energy between the particles. When the roller passes, the elastic strain energy between the particles is converted into kinetic energy, resulting in a rebound phenomenon that slightly increases the void ratio. This indicates that increasing the number of rolling passes without restriction does not further reduce porosity.

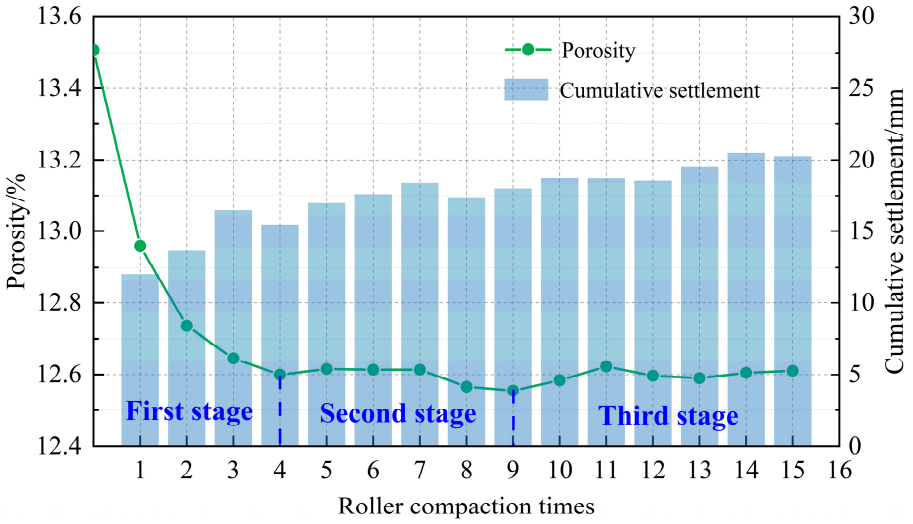


Figure 12. Porosity and cumulative settlement with increasing number of rolling passes.

4.2. Analysis of the Movement of the Rolling Model

Figure 13 is the displacement field vector diagram of the lime-mixed gravel soil and GCL under different numbers of rolling passes. Each arrow in the figure represents a single fine-grained soil particle or gravel particle, and the direction of the arrow is the direction of particle displacement. Figure 13 shows the number of particles displaced and the amount of displacement with the increase in the number of compaction times, which indicates that the number of compaction times directly affects the frequency of particle movement. As the protective layer and GCL particles are displaced, the displacement of particles in the protective layer is greater than that in the GCL layer, indicating that the particles in the middle and upper layers are easier to compact than the lower layer of particles under the action of a vibratory rolling load. The left particles move more frequently than the right particles, which is possibly due to the presence of more pores on the left side during the model settling process, and the particles are more likely to be arranged and filled under the vibration rolling load.

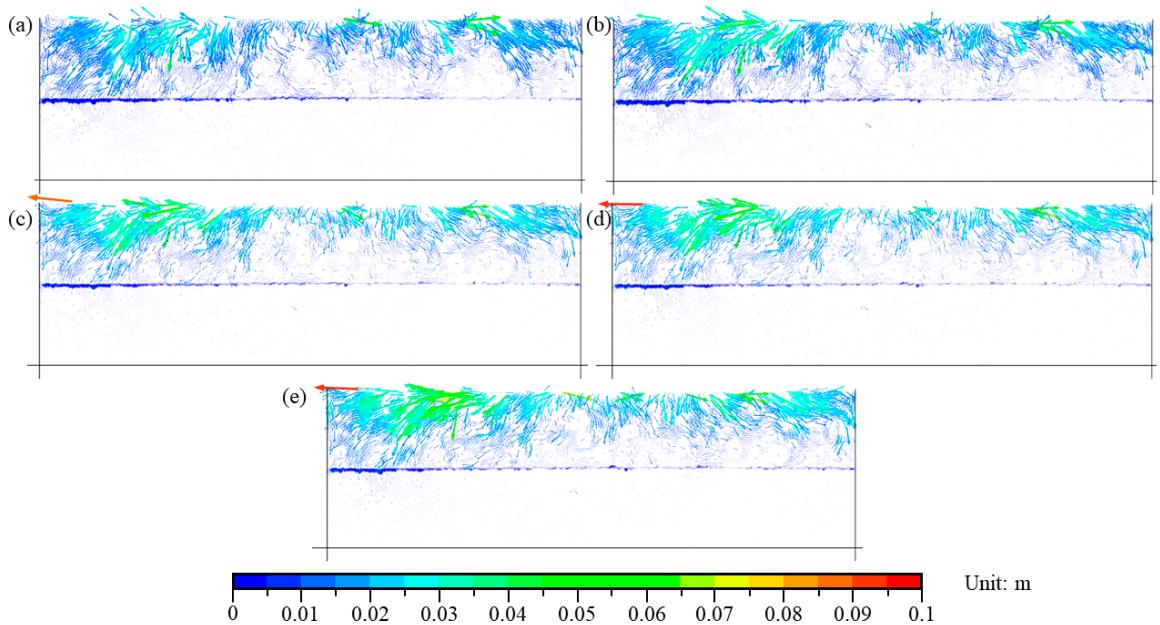


Figure 13. Vector displacement field of lime-mixed gravel soil and GCL under different numbers of rolling passes: (**a**) the fourth time; (**b**) the sixth time; (**c**) the ninth time; (**d**) the eleventh time; (**e**) the fifteenth time.

4.3. Analysis of the Movement of Gravels

To study the movement of gravels more clearly, typical gravel particles were selected in the upper, middle, and lower layers of the model to observe their movement trajectories during the rolling process. Figure 14 shows the typical gravel distribution location and gravel boundary schematic diagram. As shown in Figure 14a, the PL group reflects the gravels in the protective layer, where PL1 is the gravels directly contacting the roller at the top, and PL2 is the gravels in the upper loose part; the GL group reflects the gravels contacting the GCL; the SL group reflects the gravels in the support layer. From Figure 14b, the shapes of typical gravels can be summarized as follows: approximately circular, approximately rectangular, approximately oval, approximately triangular, or approximately trapezoidal. The gravels in the protective layer are mainly approximately circular, approximately rectangular, and approximately oval, and the gravels in the support layer are mainly approximately triangular and approximately trapezoidal.

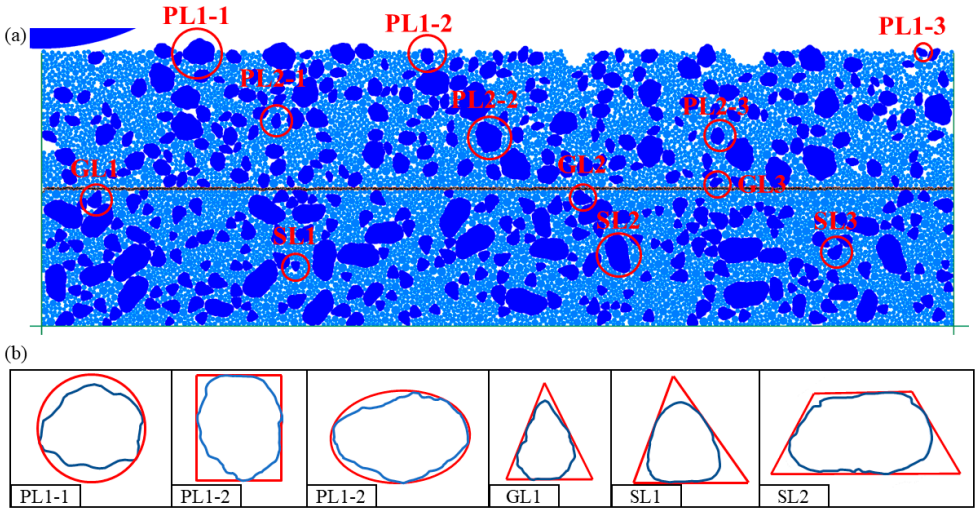


Figure 14. Typical gravel distribution and shape. (**a**) Typical gravel distribution location map; (**b**) Typical gravel shape.

Figure 15 shows the movements and trajectories of gravels in the PL group. As shown in Figure 15, the left side shows the position diagrams of gravels under different numbers of rolling passes, and the right side shows the movement trajectory diagrams of gravels in the whole rolling process. Among them, the coordinate axis range only represents the displacement range of gravels. In Figure 15a,b,d,e, the gravel movement trajectory is to the left and below, while the gravel movement trajectory shown in Figure 15d,f is to the right and below. The initial position of the protective layer gravels has a great influence on the movement trend; that is, the gravels with the initial position on the left side of the model move to the left and below, and the gravels with the initial position on the right side move to the right and below. From Figure 15a–c, the gravels all made different degrees of rotational movements during the rolling process, and there is a large change compared with the initial form after 15 rolling passes, which is because the PL1 group gravels are located at the top of the protective layer, and they are in direct contact with the roller during the compaction process and are influenced by its kneading effect. From Figure 15d–f, only PL2-1 and PL2-3 directly undergo rotational movement. The rotational frequency and displacement of this group of gravels are less than those of the PL1 group during the rolling process. The reason for this is that this group is in the middle of the protective layer, which is not in direct contact with the roller and thus is less affected by its influence, and there are fewer voids around the gravels there due to gravitational settlement. Notably, PL2-1 and PL2-3 are classified as approximately oval and approximately rectangular gravels, respectively, which shows that the probability of rotational movement of these two types of gravels in the middle of the protective layer is greater than that of approximately circular gravels.

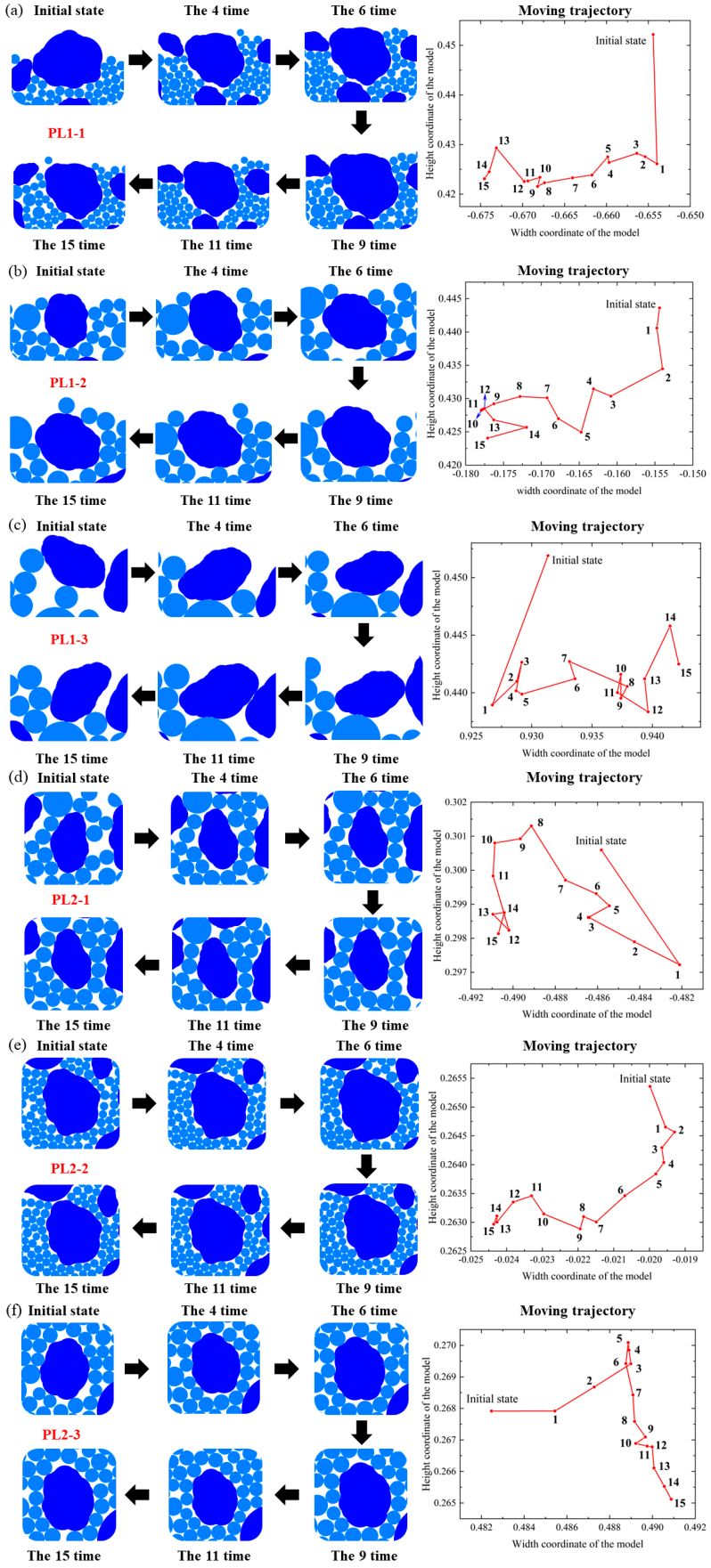


Figure 15. The movements and trajectories of gravels in the PL group: (**a**) PL1-1; (**b**) PL1-2; (**c**) PL1-3; (**d**) PL2-1; (**e**) PL2-2; (**f**) PL2-3.

Figure 16 shows the movements and trajectories of gravels in the GL group. Figure 16 shows that the direction of gravel movement in this group is random and that GL2 and GL3 gravels move upward during the rolling process. This is mainly affected by the elastic deformation energy. Under the action of gravity settlement, the number of voids here is smaller than that in the middle and upper parts of the protective layer, and the voids were filled early in the rolling process. With the increase in the number of rolling passes, the elastic deformation energy is gradually released, which is manifested by the frequent movement of fine particles to drive the gravels upward. In this group of gravels, only GL3 gravels changed in shape with the initial position after 15 rolling passes, that is, rotation movement occurred, which once again confirmed that the approximately oval gravels were easier to rotate during the rolling process.

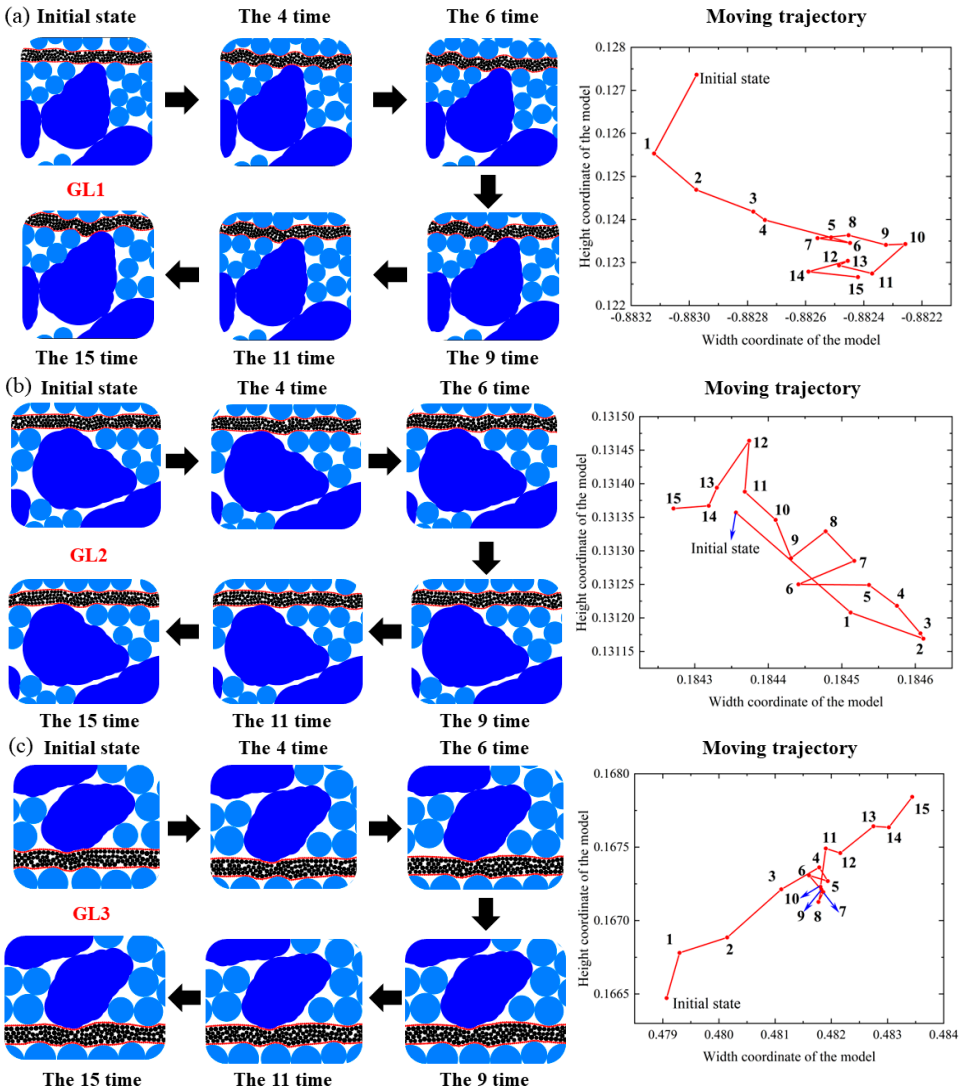


Figure 16. The movements and trajectories of gravels in the GL group: (**a**) GL1; (**b**) GL2; (**c**) GL3.

The SL group reflects the gravels in the support layer; Figure 17 shows the movements and trajectories of gravels in the SL group. Figure 17 shows that the movement direction of this group of gravels is relatively uniform, and the randomness is less than that of the SL group gravels near the GCL. Notably, only a small amount of displacement can be observed in the movement trajectory diagram of this group of gravels, so the movement pattern during the rolling process is difficult to determine. The frequency of gravel movement in the support layer is much smaller than that of the protective layer and the gravel near the GCL.

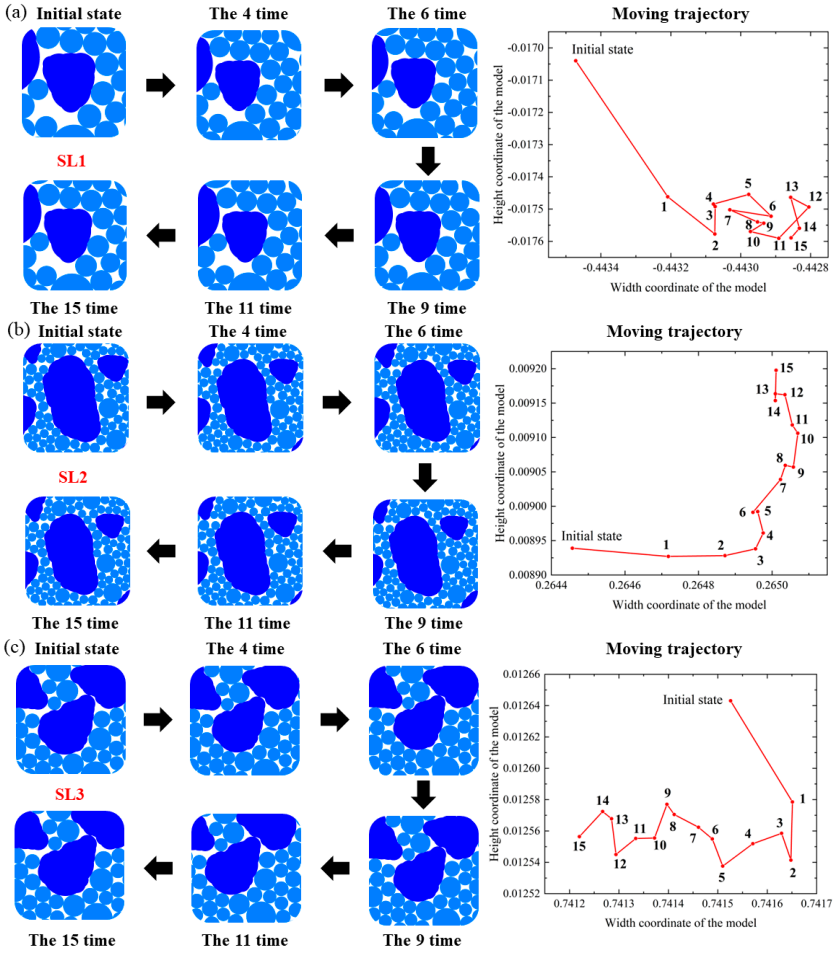


Figure 17. The movements and trajectories of gravels in the SL group: (**a**) SL1; (**b**) SL2; (**c**) SL3.

Figure 18 shows the maximum displacement and maximum rotation speed curve of typical gravels in each group. Figure 18a shows that the maximum displacement of the gravels in the SL group is much smaller than that in the PL group and the GL group, which again shows that the gravels in the middle and upper parts of the model are more easily compacted. Figure 18b shows that the maximum rotation speed of the gravels in the SL group is smaller than that of the first two groups of gravels, which confirms that the movement frequency of the gravels in the support layer is smaller than that of the gravels near the protective layer and the GCL.

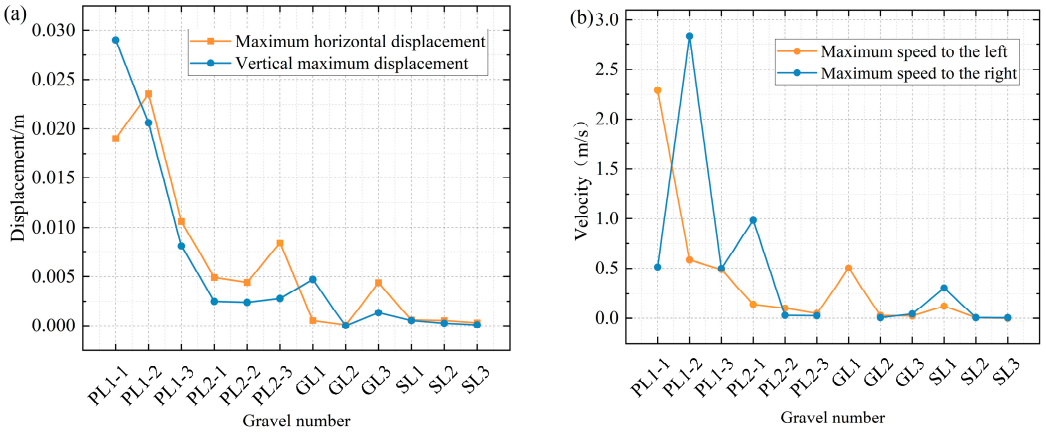


Figure 18. The maximum displacement and maximum rotation speed curves of gravels in each group: (**a**) maximum displacement; (**b**) maximum rotation speed.

4.4. The Impact of Gravels on the GCL

The previous analysis indicates that the GCL near the movement of the gravels is more active and that there is rotational movement. This movement may cause extrusion, jacking, and embedment in the GCL and other effects. To explore this problem, typical gravels (A/B/C/D/E) are selected near the GCL for research. Figure 19 shows a typical gravel and GCL contact point displacement map obtained during the rolling process.

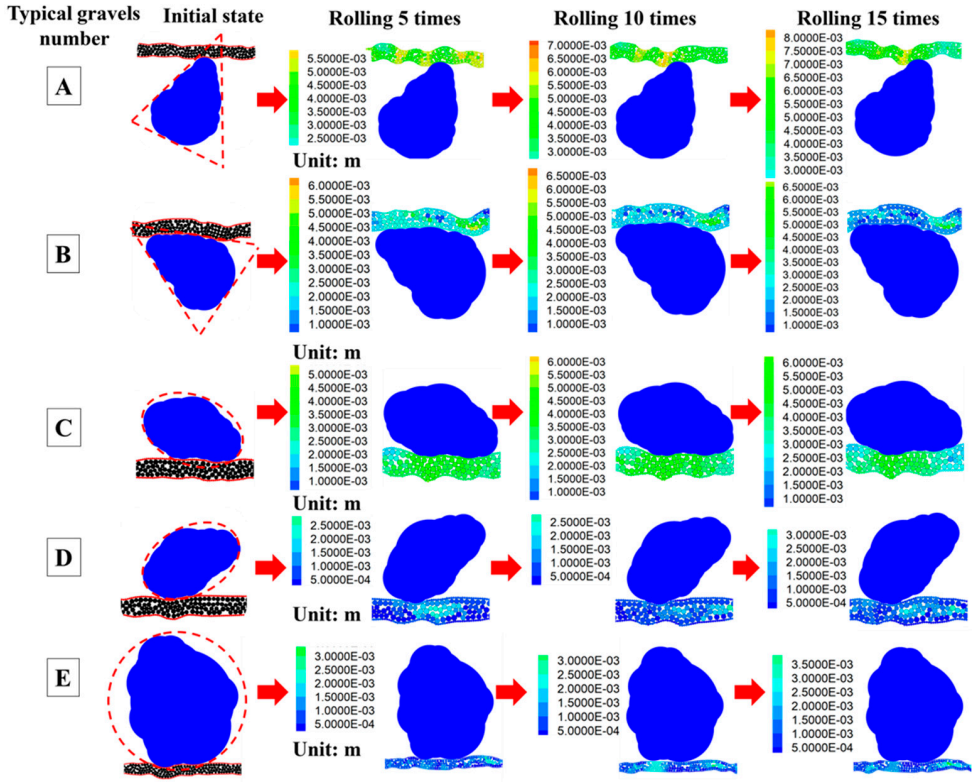


Figure 19. Displacement diagram of the contact points between typical gravels and the GCL during the rolling process.

As shown in Figure 19, the impact of gravel movement on the GCL increases with the number of rolling passes, and the gravels' location and shape have different effects on the impact on the GCL. As shown for A and B, the approximately triangular gravel and GCL contact state has two cases: one is the point contact between the corner and the GCL, and the other is the surface contact between the edge and the GCL. The former has the obvious phenomenon of squeezing the GCL, and there is a risk of puncture; the latter contact area is large. Although the risk of puncture is small, the GCL may be punctured during the compaction process, causing the bentonite to move to both sides and weakening the anti-seepage effect of the contact position. As shown for C and D, the approximately oval gravel and GCL contact state also has two cases, that is, the long-axis boundary contact and the short-axis boundary contact. The former is the same as the point contact of the approximately triangular gravel, and the latter is the same as the surface contact of the approximately triangular gravel. In Figure 19, E shows that the approximately circular gravel and GCL contacts mainly occur as face contacts, with the overall extrusion of the GCL.

5. Quality Evaluation Index of GCL After Rolling Construction

In the rolling process, the influence of gravel displacement on the GCL cannot be ignored. Therefore, taking the influence of different factors on the GCL in the construction process as the starting point, the local elongation of the GCL, the embedding value of gravels, and the coordination number of the bentonite were adopted as three evaluation indexes to describe its integrity and the impermeability effect.

5.1. Local Elongation of the GCL

To analyze whether tensile damage occurs in the GCL during the rolling process, the local elongation was defined to calculate the values under different rolling states, and the maximum elongation of the GCL was calculated and verified. Figure 20 shows the local length of the GCL.

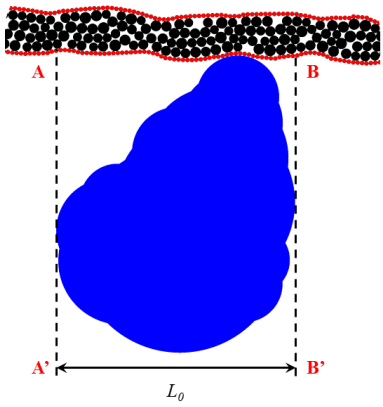


Figure 20. Local length diagram of the GCL.

As shown in Figure 20, in the initial state, the maximum diameter A'B' in the horizontal direction of the gravel is projected onto the GCL, and the corresponding projected length AB on the GCL is considered the local length L_0. During the rolling process, the GCL will be stretched or shrunk, that is, the length of AB will change. Thus, the local length of the GCL after different numbers of rolling passes is defined as $L_i(i = 1, 2, \ldots, 15)$, and the local elongation is calculated as follows (Equation (6)):

$$\delta = (L_0 - L_i)/L_0 \tag{6}$$

where δ is the local elongation of the GCL; L_0 is the local length of the GCL; and L_i is the local length of the GCL after different numbers of rolling passes.

5.2. Embedding Value of Gravels

Taking the contact between the gravels and GCL shown in Figure 19 as an example, the results of the local elongation calculation are shown in Figure 21. Except for gravel B, the local elongation of the GLC with other gravels increases with the number of rolling passes, and the maximum value is 3.79%, which is less than the maximum tensile rate of the GCL (14%). The GCL undergoes different degrees of stretching during the rolling process but never exceeds the maximum limit value, indicating that the integrity is good during the construction process.

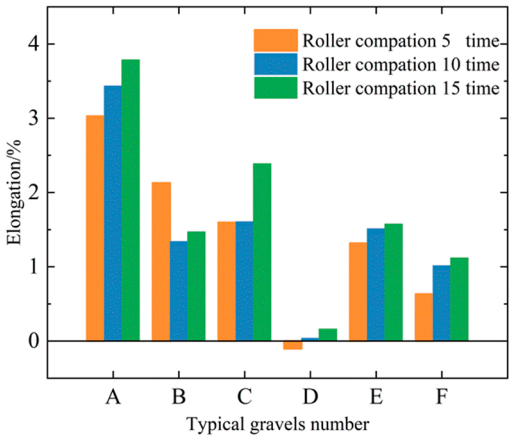


Figure 21. Local elongation of the GCL under actual working conditions.

The definition of the gravel embedding value is shown in Figure 22. It refers to the distance between the lowest point of the gravel in contact with the upper boundary of the GCL during the rolling process and the initial height of the GCL.

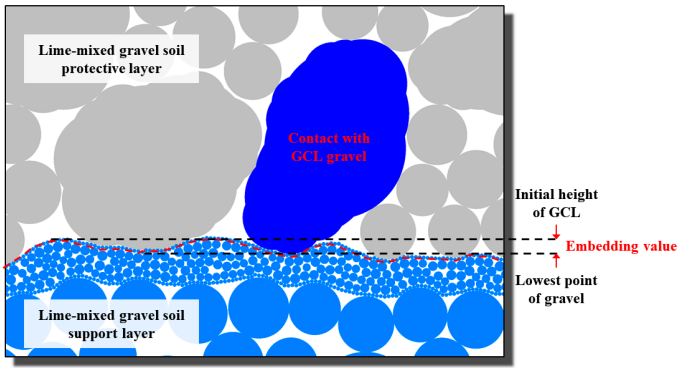


Figure 22. Definition of gravel embedding value.

The embedding value of the gravels is calculated with Equation (7):

$$z_e = \overline{z}_g - z_{p\min} \tag{7}$$

where z_e is the gravel embedding value. $\overline{z}_g$ is the average initial height of the GCL. $z_{p\min}$ is the longitudinal coordinate of the lowest point of the gravel in contact with the GCL, and $\overline{z}_g$ is calculated from Equation (8).

$$\overline{z}_g = \sum_{i=1}^{n} z_{gi}/n \tag{8}$$

where z_{gi} is the height of the GCL particles and n is the number of GCL particles.

According to Equations (7) and (8), the variation in the depth of gravel embedded in the GCL with the number of rolling passes is shown in Figure 23. As shown in Figure 23, the embedding value of the gravels increases overall during the rolling process, but the embedding value of some of the gravels fluctuates in the process of increasing, indicating that the gravels near the GCL have high movement frequencies and complex movement trajectories under the action of a vibration rolling load. At the same time, the GCL will move in a "wave" motion after being squeezed, which makes some gravels move upward under the swing of the GCL, resulting in a decrease in the embedding value, which is also one of the reasons for the fluctuation in the embedding value of some gravels. The trend of the change curve of the embedding value is the same as the changing trend of the porosity. When rolling the first time, the embedding value of the gravel increases rapidly, and the change tends to be stable with the increase in the number of rolling passes. The final embedding value is nonzero, indicating that the gravels are embedded in the GCL.

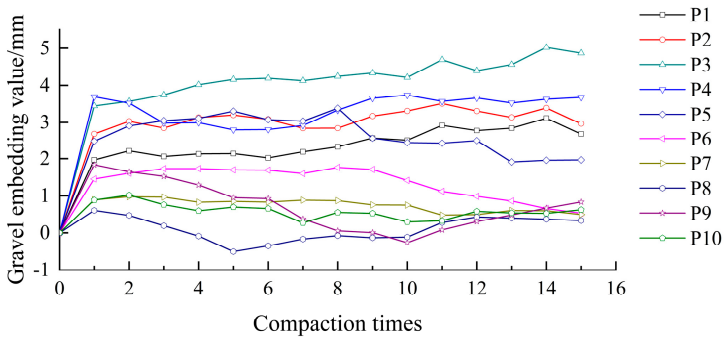


Figure 23. The change in gravel embedding value with the number of rolling passes.

5.3. Distribution of Coordination Number of Bentonite

During the rolling process, the distribution of bentonite can be analyzed by monitoring the change in the coordination number of the bentonite particles. The coordination number refers to the average contact number of particles in the measurement range. The larger the coordination number, the more contact around the particles, indicating that the particle density in this area is higher and the structure is more stable. Figure 24 shows a typical measurement point selected to measure the distribution of bentonite particles in the GCL. As shown in Figure 24, the typical contact position can be divided into three cases: A for two adjacent gravels squeezing the GCL at the same time, B for more than one gravel squeezing the GCL vertically, and C for larger gravels squeezing the GCL.

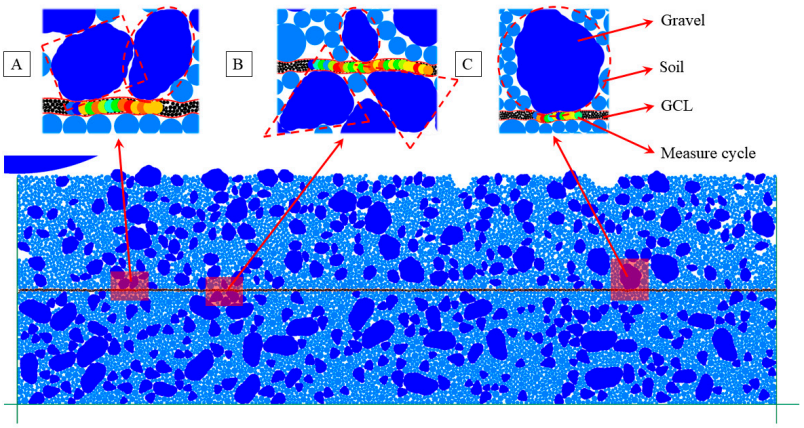


Figure 24. Observation points of the distribution of coordination number of bentonite.

Figure 25 shows how the coordination numbers of bentonite particles at typical contact positions change during the whole rolling process. The bubble size is proportional to the coordination number. If the coordination number increases, the number of particle contacts in the measurement circle increases. From a macroscopic point of view, many bentonite particles can adsorb a large amount of water to achieve the effect of impermeability when the water flows through; on the other hand, if the coordination number decreases, it indicates that the number of particle contacts is small, i.e., the bentonite particles move frequently under the effect of rolling, resulting in a decrease in the number of bentonite particles there. The coordination numbers monitored at the G, H, I, and J circles in Figure 25a and the I, J, K, N, and R circles in Figure 25b fluctuate greatly, indicating that the bentonite particles move frequently during the rolling process, whereas the coordination number in Figure 25c is evenly distributed, indicating that the bentonite particles are dense during the rolling process. When the approximately circular gravels are in contact with the GCL, the overall movement of the bentonite particles is uniform and orderly; when two or more gravels are distributed on the same side or opposite sides, it is easy to squeeze the GCL so that the bentonite particles move frequently. Figure 26 is the schematic diagram of the GCL change. As shown in Figure 26a, the bentonite particles are affected by the extrusion of the gravel surface contact. Compared with the initial state, the bentonite particles in the extruded part move to both sides. Although the number of particles in the same area decreases, the particles are still in close contact. As shown in Figure 26b, due to the influence of gravel point contact, the GCL moves frequently, and the movement of the boundary in the vertical direction leads to the diffusion of bentonite particles. Currently, the number of particle contacts is reduced, and the anti-seepage effect is weakened. In the simulation process, it is found that, in the first case, it is necessary to detect the local elongation of the GCL. If it is less than the maximum elongation, the GCL is structurally safe. The second situation is due to the rolling speed being too fast, causing more gravels and GCL point contacts; so, selecting the appropriate rolling speed for the actual construction process while paying attention to the distribution of gravels is important to prevent the diffusion of bentonite particles, which reduces the anti-seepage effect.

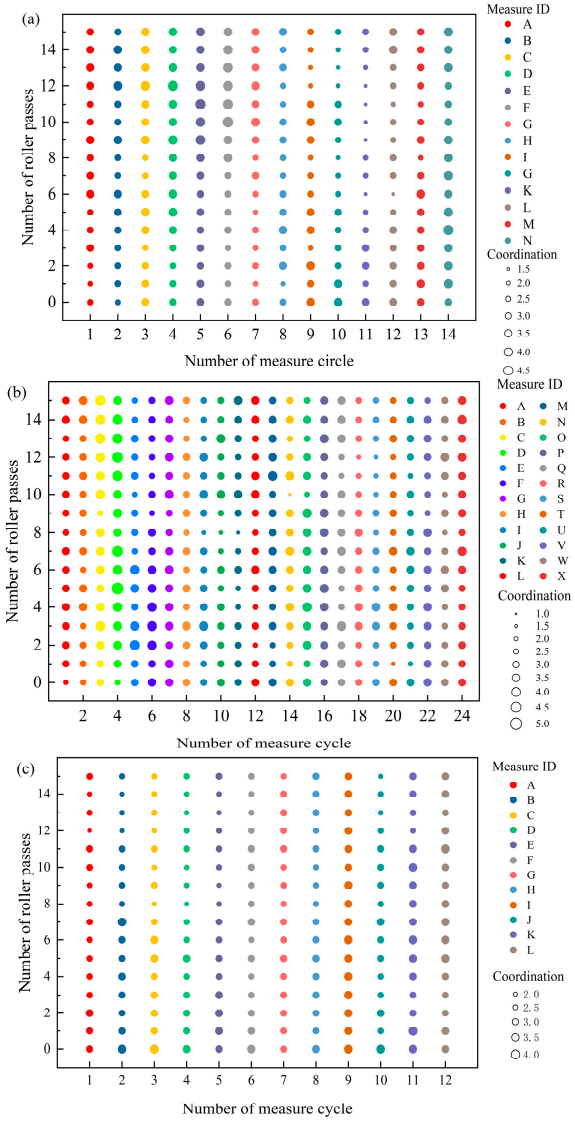


Figure 25. The change in the coordination number at the typical position of the gravel–GCL contact during rolling: (**a**) A contact position; (**b**) B contact position; (**c**) C contact position.

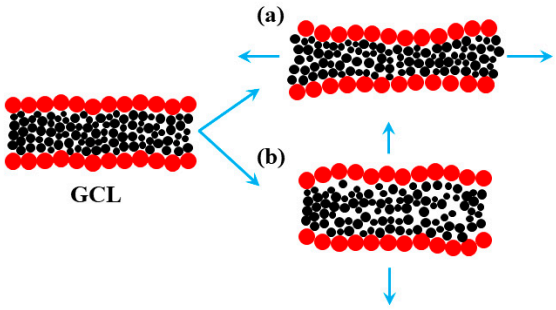


Figure 26. Schematic diagram of GCL changes. (**a**) Effect of gravel surface contact on bentonite particles; (**b**) Effect of gravel point contact on bentonite particles.

6. Conclusions

In this study, a vibratory compaction construction model of a lime-mixed gravel soil support layer–GCL–protection layer was constructed using a DEM numerical simulation method and in combination with test results. The compaction characteristics of lime-mixed

gravel soil and the effect of gravel migration on GCL were explored at the mesoscopic level. The main conclusions are summarized below:

(1) A fine vibratory rolling construction model of a high-precision lime-mixed gravel soil support layer–GCL–lime-mixed gravel soil protection layer, considering an irregular gravel shape and actual excitation force, was established in combination with indoor experiments, and the accuracy of the rolling construction model was improved.
(2) Through the analysis of the dynamic simulation of the rolling construction process, it is concluded that with the increase in the number of rolling passes, the porosity and cumulative settlement show the trend of rapid decline–gentle decline–slight change–stability, and 8~9 rolling passes are recommended according to the DEM simulation results.
(3) The migration laws of different shapes of gravels at different locations were revealed. During vibratory crushing, the near-rectangular and near-elliptical gravels are prone to rotation, and the movement frequency of the gravels decreases with the increase in gravel burial depth. The gravel in the upper protective layer has the highest frequency of movement and the direction of movement is uniform. The gravels near the GCL layer have a higher frequency of movement than the gravels near the support layer, but the direction of movement is complex and random. The lower support layer has the lowest movement frequency.
(4) According to the movement pattern of irregular gravels in the upper and lower layers of the GCL, there is a mutual influence between gravels and the GCL. The contacts of the approximately triangular and approximately oval gravels and the GCL are mainly point contacts and surface contacts. The approximately circular gravels are in surface contact with the GCL. The discovery of different contact forms provides sup-port for subsequent research on the microscopic mechanism of GCL gravel extrusion.
(5) Three evaluation indexes, local elongation of the GCL, embedding value of the gravels, and coordination number of the bentonite, were systematically proposed. The maximum local elongation at the five contact positions studied in this paper is 3.79%, which is less than the design specification value of 14%. The gravel embedding value varies with the shape of the gravel, the contact mode, and the state of motion, and the maximum embedding value is 4.9 mm. The distribution of bentonite coordination number in GCL is closely related to the contact form of the gravel.

Author Contributions: Methodology, R.L.; Writing—original draft, F.C.; Writing—review & editing, Q.Q.; Supervision, H.H.; Project administration, L.G.; Funding acquisition, L.G. All authors have read and agreed to the published version of the manuscript.

Funding: This work was funded by the Key project of science and technology of Henan province in China (Grant no. 192102310224). The authors would also like to acknowledge the support received from the National Natural Science Foundation of China (Grant no. 52109154). The 2022 Open Fund-funded Project of the State Key Laboratory of Hydraulic Engineering Simulation and Safety of Tianjin University (No. HESS-2230).

Data Availability Statement: Data are contained within the article.

Conflicts of Interest: The authors declare no conflict of interest.

References

1. Afzali-Nejad, A.; Lashkari, A.; Shourijeh, P.T. Influence of particle shape on the shear strength and dilation of sand-woven geotextile interfaces. *Geotext. Geomembr.* **2017**, *45*, 54–66. [CrossRef]
2. Hoai, T.T.; Mukunoki, T.; Ha, N.T.H.; Nhuan, M.T. Investigation of initial hydration and rehydration of geosynthetic clay liners from sandy subgrades via X-ray computed tomography images. *Geotext. Geomembr.* **2023**, *51*, 188–200. [CrossRef]
3. Mukunoki, T.; Sato, K.; Fukushima, J.; Shida, K.; Take, W.A. Investigating the mechanism of downslope bentonite erosion in GCL liners using X-ray, C.T. *Geotext. Geomembr.* **2019**, *47*, 75–86. [CrossRef]
4. Weerasinghe, I.A.; Gallage, C.; Dawes, L. Effect of overburden confining stress on hydraulic performance of geosynthetic clay liners (GCLs). *Heliyon* **2021**, *7*, e05770. [CrossRef]

5. Sawada, Y.; Nakazawa, H.; Take, W.A.; Kawabata, T. Full scale investigation of GCL damage mechanisms in small earth dam retrofit applications under earthquake loading. *Geotext. Geomembr.* **2019**, *47*, 502–513. [CrossRef]
6. Dickinson, S.; Brachman, R.W.I. Deformations of a geosynthetic clay liner beneath a geomembrane wrinkle and coarse gravel. *Geotext. Geomembr.* **2006**, *24*, 285–298. [CrossRef]
7. Dickinson, S.; Brachman, R.W.I. Permeability and internal erosion of a GCL beneath coarse gravel. *Geosynth. Int.* **2010**, *17*, 112–123. [CrossRef]
8. Fox, P.J.; Battista, D.J.D.; Mast, D.G. Hydraulic performance of geosynthetic clay liners under gravel cover soils. *Geotext. Geomembr.* **2000**, *18*, 179–201. [CrossRef]
9. Pillai, A.G.; Gali, M.L. New perspectives on bentonite hydration and shear strength of GCL-sand interfaces based on particle shape characterizations. *Int. J. Geosynth. Ground Eng.* **2022**, *8*, 25. [CrossRef]
10. Hou, J.; Li, H.; Liu, L.; Wang, S.H.; Teng, Y.Y.; Bao, S.F. A DEM analysis of geomembrane-lined landfill subject to vertical loading. *Geotext. Geomembr.* **2021**, *49*, 369–375. [CrossRef]
11. Pillai, A.G.; Gali, M.L. Role of particle shape on the shear strength of sand-GCL interfaces under dry and wet conditions. *Geotext. Geomembr.* **2022**, *50*, 262–281. [CrossRef]
12. Chen, Y.; Jaksa, M.B.; Kuo, Y.L.; Scott, B.T. Discrete element modelling of the 4-sided impact roller. *Comput. Geotech.* **2021**, *137*, 104250. [CrossRef]
13. Cui, W.; Liu, G.F.; Song, H.F.; Wang, C. Mesoscopic Analysis of the Compaction Characteristics of Rockfill Materials Considering Gradation Shape. *Int. J. Geomech.* **2023**, *23*, 04023162. [CrossRef]
14. Liu, D.H.; Xia, X.T.; Sun, L.F. Movement and embedding characteristics of interlayer aggregates during roller-compacted concrete compaction process using discrete element simulation. *Constr. Build. Mater.* **2020**, *249*, 118765. [CrossRef]
15. Wu, K.; Sun, W.C.; Liu, S.Y.; Huang, H.B. Discrete element modeling of vibration compaction effect of the vibratory roller in roundtrips on gravels. *J. Test. Eval.* **2021**, *49*, 3869–3884. [CrossRef]
16. Li, Y.; She, C.X.; Jiao, X.L. A new method for simulating rockfill roller compaction using particle flow code. *Rock Soil Mech.* **2017**, *38*, 3029–3038. (In Chinese) [CrossRef]
17. Pei, T.; Yang, X.M. Compaction-induced stress in geosynthetic-reinforced granular base course—A discrete element model. *J. Rock Mech. Geotech. Eng.* **2018**, *10*, 669–677. [CrossRef]
18. Acquah, K.; Chen, Y. Discrete Element Modelling of Soil Compaction of a Press-Wheel. *AgriEngineering* **2021**, *3*, 278–293. [CrossRef]
19. Chen, Y.; Jaksa, M.B.; Scott, B.T.; Kuo, Y.L. Numerical investigation of the performance of the 3-sided impact roller. *Comput. Geotech.* **2023**, *157*, 105331. [CrossRef]
20. Hu, C.; Gao, J.W.; Zhang, M.; Tan, X.H. Numerical simulation of rigid tire-soil interaction based on discrete element method. In Proceedings of the International Conference on Computational Modeling, Simulation, and Data Analysis (CMSDA 2021), Zhuhai, China, 2–4 December 2022. [CrossRef]
21. Liu, D.H.; Ma, H.Y.; Sun, L.F. Determination of equivalent loads on downsized rollers in DEM simulation of rock-fill dams. *J. Hydroelectr. Eng.* **2018**, *37*, 93–102. (In Chinese) [CrossRef]
22. Liu, D.H.; Sun, L.F.; Ma, H.Y. Process Simulation and Mesoscopic Analysis of Rockfill Dam Compaction Using Discrete Element Method. *Int. J. Geomech.* **2020**, *20*, 04020047. [CrossRef]
23. Liu, Y.; Qian, Z.D.; Yang, Y.M.; Gong, M.H.; Huang, Q.B.; Zhang, X.F. Investigation on segregation characteristics of thermosetting epoxy asphalt mixture during the compaction. *Constr. Build. Mater.* **2022**, *320*, 126256. [CrossRef]
24. Lu, J.F.; Li, D.; Xue, X.Q.; Ling, S.L. Macro-Micromechanical Properties of Sandy Pebble Soil of Different Coarse-Grained Content. *Earth Sci. Res. J.* **2018**, *22*, 65–71. [CrossRef]
25. Nie, Z.H.; Qi, Q.; Wang, X.; Zhu, Y.G. DEM investigation of strain behaviour and force chain evolution of gravel–sand mixtures subjected to cyclic loading. *Particuology* **2022**, *68*, 13–28. [CrossRef]
26. Tu, Y.L.; Wang, X.C.; Lan, Y.Z.; Wang, J.B.; Liao, Q. Mechanical properties and failure mechanism of gravelly soils in large scale direct shear test using DEM. *Geomech. Eng.* **2022**, *30*, 27–44. [CrossRef]
27. *JG/T 193-2006*; Sodium Bentonite Geosynthetic Clay Liner. Standards Press of China: Beijing, China, 2006.
28. *GB/T 15788-2017*; Geosynthetics-Wide-Width Tensile Test. Standards Press of China: Beijing, China, 2017.

Disclaimer/Publisher's Note: The statements, opinions and data contained in all publications are solely those of the individual author(s) and contributor(s) and not of MDPI and/or the editor(s). MDPI and/or the editor(s) disclaim responsibility for any injury to people or property resulting from any ideas, methods, instructions or products referred to in the content.